PROCEEDINGS, 49th Workshop on Geothermal Reservoir Engineering
Stanford University, Stanford, California, February 12-14, 2024
SGP-TR-227

Investigating Reinjection Strategies to Optimise Lithium Production from the Salton Sea Geothermal Field

John O'Sullivan, Naod Araya, Joris Popineau, Theo Renaud, Jeremy Riffault and Mike O'Sullivan

Department of Engineering Science, University of Auckland, Private Bag 92019, Auckland, New Zealand

jp.osullivan@auckland.ac.nz

Keywords: Geothermal reservoir simulation, Waiwera, Salton Sea, Lithium

ABSTRACT

The Salton Sea Geothermal Field (SSGF) is one of the largest geothermal resources in the world with an estimated resource potential of nearly 3 GW (Kaspereit et al., 2016). It has only been partially exploited due to its high salinity and partial coverage by the Salton Sea. Stakeholders are now focused on better exploiting the field for geothermal energy production and using the lithium-rich geothermal brine as a source of lithium for battery production.

This modeling study uses our existing numerical model of the SSGF to investigate different options for optimising the extraction of lithium from the system. Our model of the SSGF has a chloride-NCG-water equation of state with lithium represented as a passive tracer (Araya and O'Sullivan, 2022, Dobson et al., 2023, O'Sullivan et al., 2023a). The model uses a dual porosity approach for the production history and future scenarios to provide an accurate representation of reinjection returns and chemical breakthrough by dilute lithium reinjection fluid. Publicly available data has been used to calibrate both the natural state and production history models.

Future scenarios were run to investigate the influence of the location of reinjection wells on both pressure support and lithium concentrations in produced geothermal brine. They show that lithium production can be enhanced without adversely affecting energy production by careful targeting of reinjection. The results of the simulations show the importance of careful monitoring, robust modelling and detailed planning in supporting the extraction of lithium from the SSGF.

1. INTRODUCTION

The Salton Trough is an active pull-apart basin straddling the Pacific and North American Plates in Southern California. This continental rift zone is characterized by a series of right-stepping dextral faults that link the East Pacific Rise to the San Andreas fault system (Dorsey, 2006). In the extensional gaps between these step-over faults there are a series of smaller spreading centers bounded by northwest-trending strike-slip faults and northeast-trending normal faults (Hulen et al., 2002). The historical development of the Trough is discussed in O'Sullivan et al. (2023a).

Due to crustal thinning and deep magmatic intrusions, the entire Salton Trough experiences an abnormally high heat flux of >100 mW/m2 (Lachenbruch et al., 1985). Even higher heat flows of >500 mW/m2 are concentrated in Salton Sea Geothermal Field due to localized Quaternary volcanism and upwelling of hydrothermal fluids (Sass et al., 1984). As a result, significant metamorphic and hydrothermal alteration of the Colorado River sediment occurs at shallower depths in the SSGF (~1.5 km) compared to the rest of the valley (~3 km) (Han et al., 2016).

The brine of the Salton Trough is distinguished by a bimodal distribution of salinity. Cooler less saline brine (<10 wt.% TDS) overlays hot hypersaline brine (>20 wt.% TDS). The hypersaline brines tend to be Na-Ca-K chloride solutions with high concentrations of dissolved metals (Fe, Mn, Zn, Li, Sr) while the less saline brines are typically NaCl solutions with very little dissolved metals (McKibben et al., 1987). These lower salinity brines have chemical compositions very similar to water from the New River and the Salton Sea. While the hypersaline brines have a narrower range of isotopic compositions. Williams and McKibben (1989) state this indicates active convection and a relatively long residence time.

2. CONCEPTUAL MODEL

This research seeks to characterize and forecast the recoverable lithium potential of the field by building upon our existing 3D conceptual and numerical model (Araya and O'Sullivan, 2022, Dobson et al., 2023, O'Sullivan et al., 2023a). The fundamental research questions that must be answered to assess the sustainable extraction of lithium and energy from the SSGF are as follows:

- How do the hot geothermal plume and hypersaline zone interact?
- What are the likely permeability controls on the geothermal plume and hypersaline zone?
- How can the permeability/porosity distribution of the system be exploited to maximise extraction of lithium and energy?

To answer these questions requires the development of an integrated and robust numerical model. The model needs to fully represent the latest geoscientific understanding of the system and be capable of making detailed forecasts of production and injection of chloride and lithium-rich geothermal brine. Modeling concepts and workflows described by O'Sullivan et al. (2000), O'Sullivan et al. (2016), Popineau

et al. (2018), and O'Sullivan et al. (2023b) as well as Leapfrog Geothermal software, were used to create a combined geology, alteration, and structural model.

Based on previous work by Wagoner (1980), Dorsey (2006), Dorsey et al. (2011), Kirby et al. (2007), and Hulen et al. (2003), the following seven geologic units were modeled chronologically from oldest to youngest: Crystalline Basement, Imperial Group, Palm Springs Formation, Lower Borrego, Upper Borrego, Brawley Formation, and Alluvium. Regional stratigraphic cross-sections from these studies were used to establish the general thickness of each formation. The Borrego Formation was split to capture the dramatic metamorphic and seismic velocity changes that occur at ~1.5 km depths beneath the center of the SSGF. The crystalline basement surface contact was traced using a regional geological map (California Department of Conservation, 2015).

The Salton Sea sub-basin is dominated by a complex network of blind right-stepping dextral faults and R' Riedel shear faults. The modeled dextral faults include the left strand of the Brawley Fault Zone (fault I), the right strand of the BSZ (fault B), Red Hill (fault R), Calipatria (fault P), Wister (fault W), Southern San Andreas (fault A) and fault C which was inferred from the alignment of old CO2 fumaroles and wells (e.g., Svensen et al., 2007; Mazzini et al., 2011; Rao, 2016). These faults were all modeled as having near-vertical dips. They were digitized from maps provided by Kaspereit et al. (2016), Marshall et al. (2022), and Lynch and Hudnut (2008). Some interpretation was applied to assign their ultimate placement and orientation (Figure 1).

The previously mentioned fault maps in addition to one from McGuire et al. (2015) were used to digitize the R' Riedel shear faults. These faults include the Elmore Ranch (fault E), Main Central Fault Zone (fault M), Kalin (fault K), Hudson (fault H), Southern boundary (fault U), fault T, Butte 1 (fault V), Butte 2 (fault X), Butte 3 (fault Y), Butte 4 (fault Z).

Four 2D land and offshore resistivity profiles by Nichols (2009) were used to digitally construct the clay cap in the conceptual model. The clay cap was defined as the extremely conductive zone (0.2 to 0.4 Ohm-M). Some uncertainty in the location of the clay cap exists as the combination of high temperature, high salinity, and high porosity can also produce very low resistivity values (Nichols, 2009). Thus, some of the low resistivity anomalies may not actually be part of the clay cap. The landward lateral extent of the clay cap was further refined by resistivity and density maps from Younker et al. (1981). Due to the lack of 3D MT data, some interpretation was required therefore increasing the potential uncertainty in model parameters.

The conceptual model including stratigraphy, the clay cap and faults is shown in Figure 2.

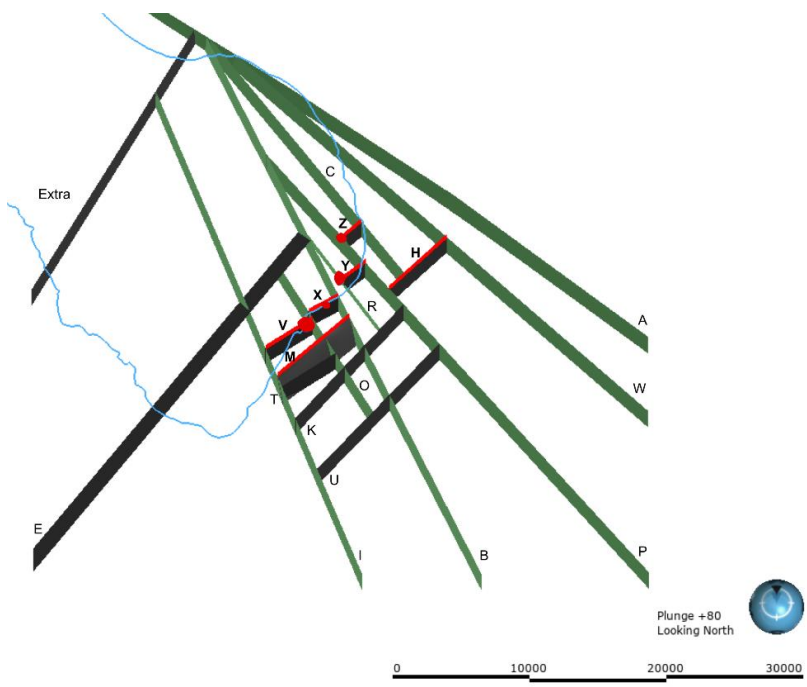

Figure 1: Faults included in the numerical model. Salton Sea (light blue) and volcanic buttes (red) as reference. Green faults are near vertical dextral faults. Black faults are R' faults with little to no upwelling. The black faults with red traces represent R' faults with significant upwelling.

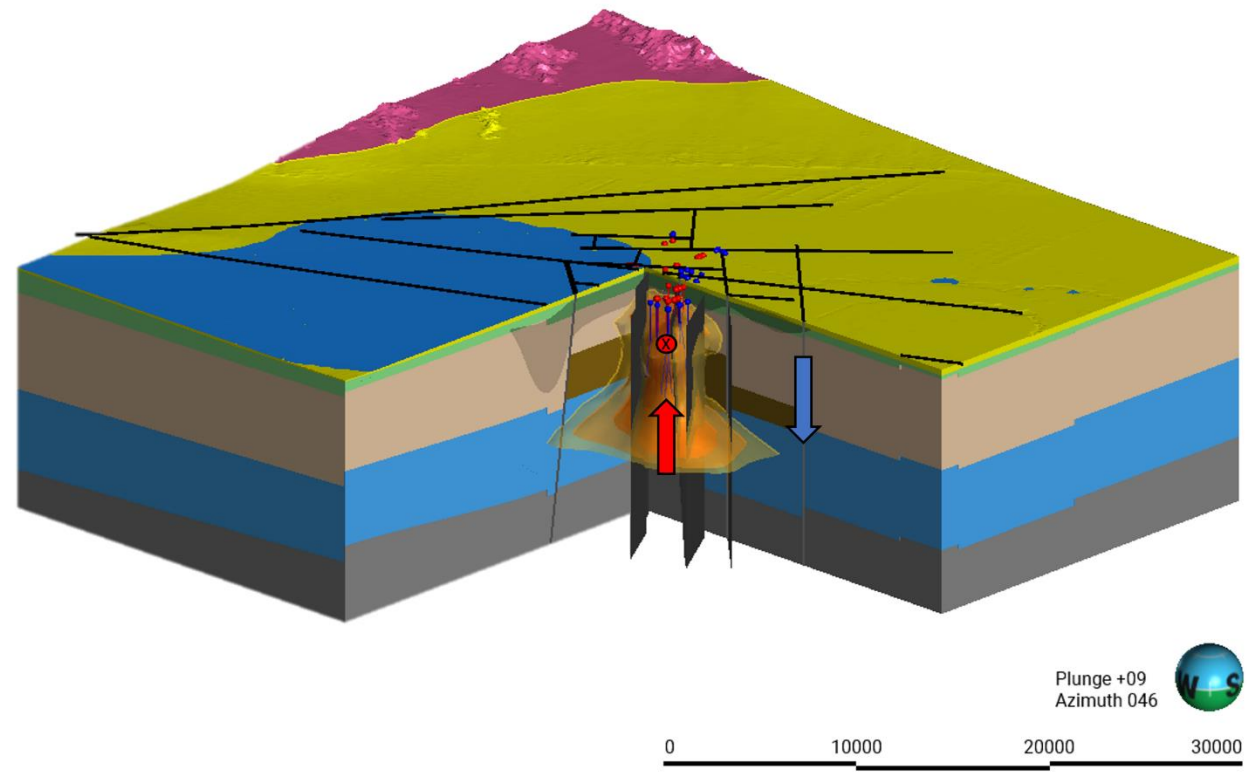

Figure 2: Conceptual model of the Salton Sea Geothermal Field. Salton Sea (blue). Geological units: Granitic Basement (pink), Imperial Formation (grey), Palm Springs (blue), Upper Borrego (tan), Lower Borrego (brown), Brawley (Green), Alluvium (yellow). Select faults shown as black surfaces. Fault traces (black). Shaded zone denotes clay cap. Active production wells (red). Active injection wells (blue). Red arrows show upflow and blue arrows show cold down flow.

3. NUMERICAL MODEL DESIGN

The 3D conceptual model was discretized into a block model for applying mass and energy balance calculations using the Waiwera geothermal simulator (Croucher et al., 2020). The model was run in the Cloud using 96 core high-performance compute nodes with Amazon Web Services (AWS).

A grid extending 24 x 24 x 3.5 km (see Figure 3) and oriented along the NE trending axis of the Main Central Fault Zone was created in Leapfrog Geothermal. The grid has a 400 x 400 m lateral refinement within the SSGF boundary and an 800 x 800m refinement on the periphery. The grid was designed with a vertical refinement of 25 m near the surface, 50 m at the water table, 100 m in the upper reservoir, 200 m in the lower reservoir, and 500 m at the greatest depths. The final numerical grid consisted of 37,688 blocks..

The EWASG equation of state in Waiwera was used to include salinity and CO_2 in the thermodynamic calculations and lithium was included in the model as a passive tracer. The top of the model was assigned dry atmospheric conditions of 1 bar and a mean temperature of 23°C on land and a wet atmosphere for the Salton Sea with a temperature of 23°C and a pressure determined by the depth of the sea. The chloride concentration of the Salton Sea was set to a mass fraction of 50,000 ppm. The side boundaries of the grid are located past all bounding faults allowing no-flow lateral boundary conditions to be applied. At the base of the model a background heat flux of 150 mW/m^2 was applied with an additional 136 MW applied as heat and mass inputs under the SSGF representing the deep geothermal upflow. Chloride was included in the deep upflow at a mass fraction equivalent to 152,000 ppm and lithium at a concentration of 220 ppm, a ratio of 682:1. The CO_2 concentrations were fixed at negligible values for all boundary conditions during this stage of the project.

The model used 561 rock-types covering the combinations of lithology, fault zone, fault zone intersections, and alteration that are included in the conceptual model. Many rock-type classifications share common permeability and porosity values, but the large number of combinations allows a high level of heterogeneity in the permeability and porosity distributions as required. Other secondary rock properties (density, heat conductivity, and rock grain-specific) were held constant across all rock-type classifications.

During production and future scenario runs, a dual-porosity model was used to capture reinjection returns more accurately. The dual-porosity parameters are given in Table 1 below.

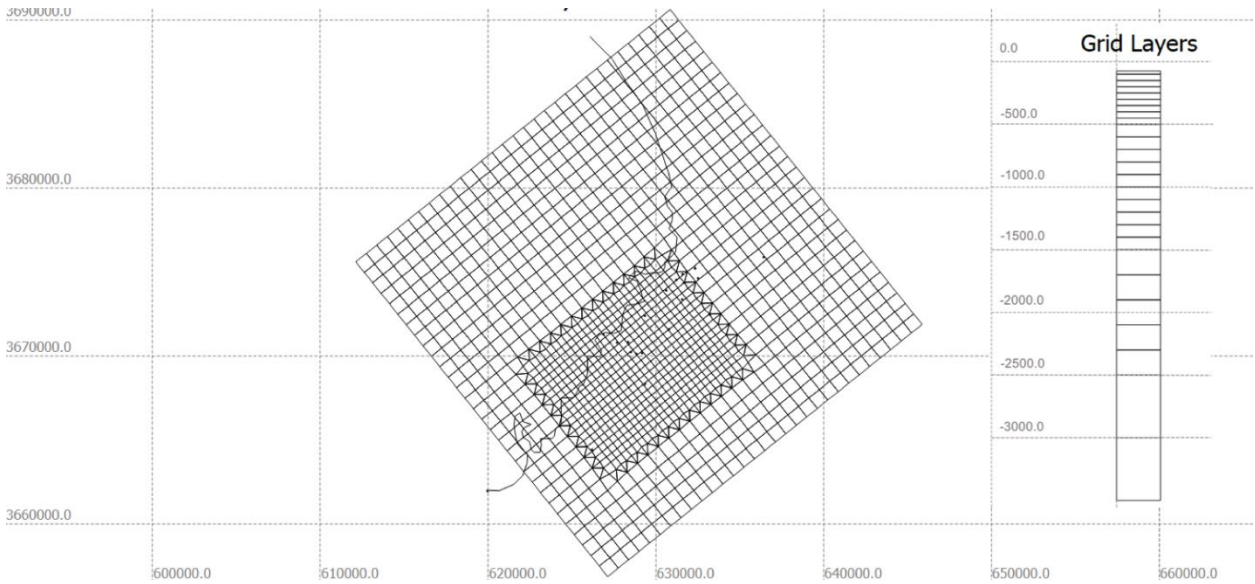

Figure 3: Map view of the model grid with the black line representing the Salton Sea shoreline. The cell size in the refined area of the grid is 400 m x 400 m, and in the coarser area it is 800 m x 800 m. The thickness of the grid layers increases with depth.

Table 1: Dual porosity parameters used in the production history model and future scenarios.

Parameter	Value
Number of matrix blocks	2 (20% and 77.5%)
Volume fraction of fracture blocks	2.5%
Fracture spacing	25 m
Fracture planes	3
Permeability of matrix	1.0E-16 m^2
Permeability of fractures	variable
Porosity of fractures	80 %

4. CALIBRATION DATA

4.1 Exploration Wells

Static temperature and brine chemistry data from exploration wells drilled prior to the start of 1980s commercial production were compiled from studies by Helgeson (1968), Palmer (1975), and Sass et al. (1988). Helgeson (1968) obtained temperature measurements over a three-year period for the following eight wells: IID 1, IID 2, IID 3, River Ranch 1, Sinclair 3, Sportsman 1, Elmore 1, and State 1. Palmer (1975) compiled temperature and brine chemistry data from MagMaMax 1, MagMaMax2, MagMaMax3, and Woolsey 1. Lastly, Sass et al. (1988) analyzed temperature data from the State 2-14 well to construct an equilibrated static temperature profile.

Static temperature surveys for Lander 2, Elmore IW-4, River Ranch 17, Fee 5, and Vonderahe 1 were collected from CalGEM's GeoSteam data repository. Most of these temperature profiles exhibit a change from a conductive to a convective gradient between depths of 600 to 900 m. This break corresponds well with the average depth of the impermeable clay cap (Sass et al., 1988).

Examples of the downhole temperature data are shown in the plots in Figure .

4.2 Active Production and Injection Wells

CalGEM's GeoSteam database was used to obtain monthly production and injection data for all the active production and injection wells in the SSGF. These monthly production/injection reports document the average monthly TDS, discharge temperature, wellhead pressure, steam mass rate, and brine mass rate. The GeoSteam database was also used to get well schematics, directional surveys, mud logs, static PTS logs, and well history reports for all the active production and injection wells. Well schematics provided wellhead coordinates, KB, ground level, and total measured depth. Total and/or partial circulation zones that were noted in the mud logs were used to infer feed zones. This was the best approach given the lack of proprietary well-testing and feed zone data.

5. NATURAL STATE MODEL

The natural state model was calibrated following standard practice by adjusting the permeability distribution and deep geothermal inputs at the bottom boundary of the model. A good model calibration (Araya and O'Sullivan, 2022) had already been achieved matching measured downhole temperatures. However, the addition of chloride significantly affected the thermodynamics of the system requiring substantial re-calibration of the enhanced model.

The plots in Figure 4 show a representative selection of modeled natural state downhole temperatures compared with measured data. Overall, the match is good though more work is required to increase deep temperatures. This is a challenging task as some measured temperatures are close to 360°C which is the limit of application for the current version of the Waiwera simulator.

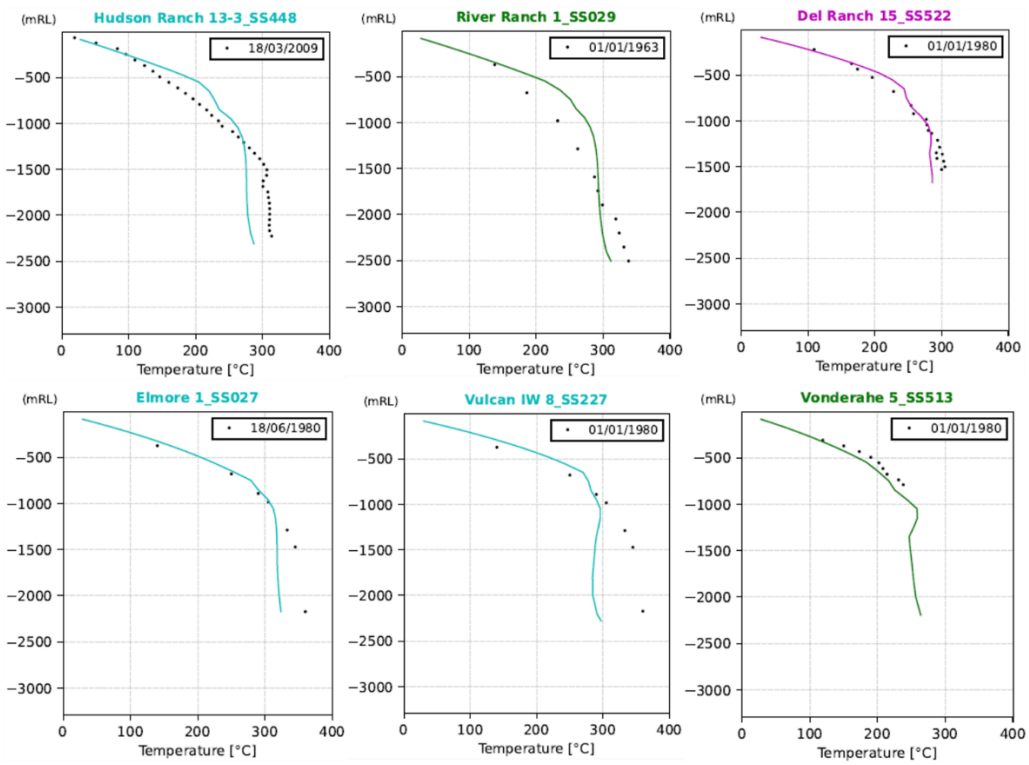

Figure 4: Natural state downhole temperatures for selected wells. Model results are shown as lines and measured data as points.

Results from the calibration process demonstrate that the infield R'Riedel shear faults and dextral strike slip faults are the main drivers of vertical upflow (see Figure 5). Hot upflow is concentrated along faults M, V, X, Y, O, and I. The reservoir is bounded in the k1 horizontal direction by faults E, T, K, and U. These R' shear faults limit outflow to the south and to the northwest. The reservoir is bounded in the k2 horizontal direction mainly by faults I, O, B, P, W, and A. The clay cap acts as an upper boundary to vertical fluid flow. The clay cap is thickest in the NW of the Sea where it acts as a lateral boundary to northeast outflow. Lastly, the periphery dextral faults (U, K, W, and A) act as large conduits for cold shallow infiltration.

As well as calibrating the temperature distribution, the model permeability distribution was adjusted to produce a chloride distribution consistent with the measured data. In particular, the aim was to reproduce the deep hypersaline reservoir overlaid with an intermediate mixing zone and a low-chloride shallow zone. Figure 6.A shows the 140,000-ppm chloride isosurface from the natural state model. Overall, it captures the deep hypersaline reservoir and the intermediate mixing zone. However, in the model the deep hypersaline fluid penetrates the shallow zone over a much larger area than has been observed. More model calibration is required, reducing permeabilities in the vertical pathways between the deep reservoir and the shallow system to reduce the upflow of hypersaline fluid. Lithium is included in the natural state model as a passive tracer with its concentration coupled closely to chloride concentration. Therefore, the lithium distribution estimated by the natural state model closely follows the chloride distribution as can be seen in Figure B.

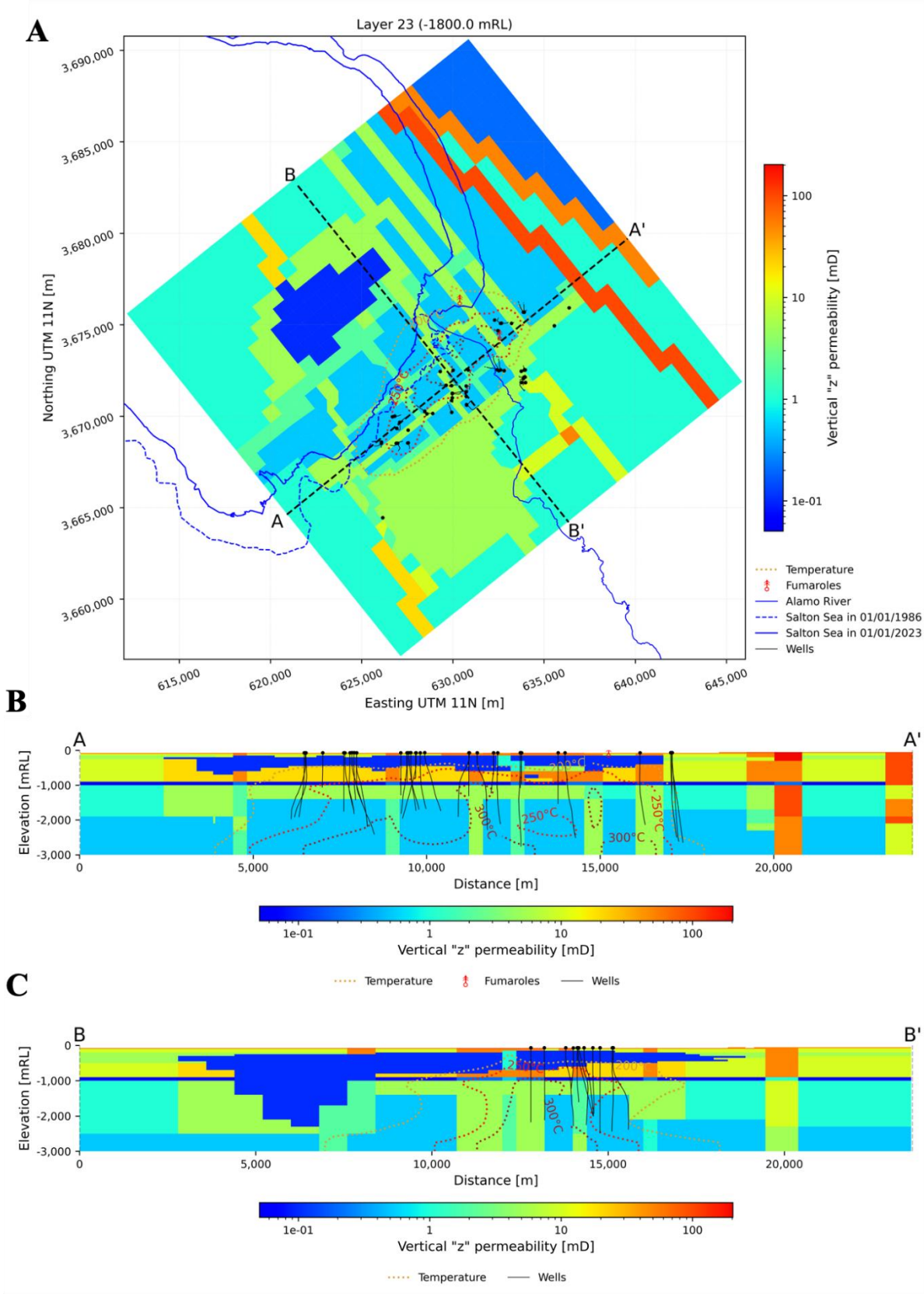

Figure 5: Vertical permeability distribution of model. 300□C, 250□C, and 200□C isotherms shown as maroon, red, and orange dotted lines, respectively. Well tracks (black). A) Horizontal slice at -1800 mRL with A to A' and B to B' slice locations. B) A to A' vertical slice. C) B to B' vertical slice.

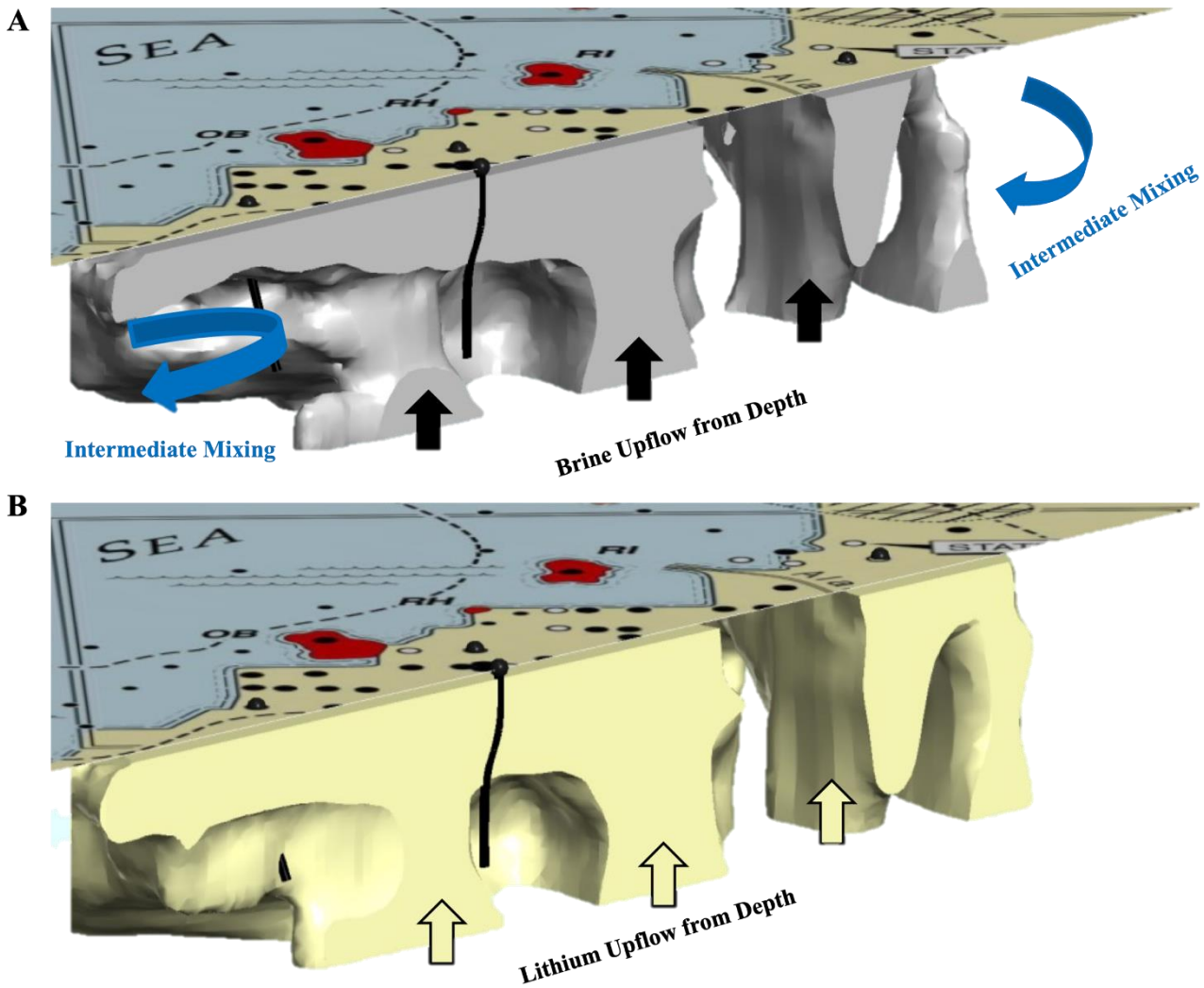

Figure 6: A) Natural state model estimated 140,000 ppm chloride isosurface. B) Estimated 170 ppm lithium isosurface.

6. PRODUCTION MODEL

The production model was set up using our standardized framework for including production and reinjection wells (O'Sullivan et al., 2023). This approach adds wells as time dependent source and sink terms in the model blocks corresponding to the feed zones of the production and reinjection wells. The model was then run for the corresponding production history time period and calibrated to match measured transient data for production enthalpies and chloride mass fractions. For the reinjection wells the enthalpy of the reinjected fluid and its chloride concentration are model inputs taken from measured data. The lithium concentration for the reinjection fluid was assumed to remain constant at a ratio of 682:1 to the measured chloride, as no appreciable lithium has historically been extracted from the brine.

Examples of measured data and production model results for selected production and reinjection wells are shown in Figure and 8. Each figure has a map in the upper left showing the location of the well. The results for the production well are typical with the measured chloride concentration increasing over time and a gentle decline in production enthalpy.

The plots in Figure indicate breakthrough of the higher chloride concentration and lower enthalpy reinjection fluid. The model results for the selected production well match the measured data very well and it shows that the model forecasts an increasing lithium production concentration also due to the higher lithium concentration in the reinjected fluid than in the reservoir.

The rate of thermal and chemical breakthrough as a result of reinjection is dependent on the permeability and porosity distributions, the location of the production and the reinjection wells and their feedzones, and the rates of production and reinjection. Figure 9 shows the model representation of the chloride distribution at 2023 as a result of 40 years of geothermal production and reinjection. Its shows the increased chloride concentrations are distributed heterogeneously across the field as a result of faults, formations and differences in production and reinjection elevations. The current model does a good job of matching the overall behavior of the SSGF and the dual-

porosity approach allows a good representation for the reinjection returns. However, more calibration, more detailed calibration data and a more refined model grid would allow for more accurate representation of the historic changes in the chloride and lithium concentrations.

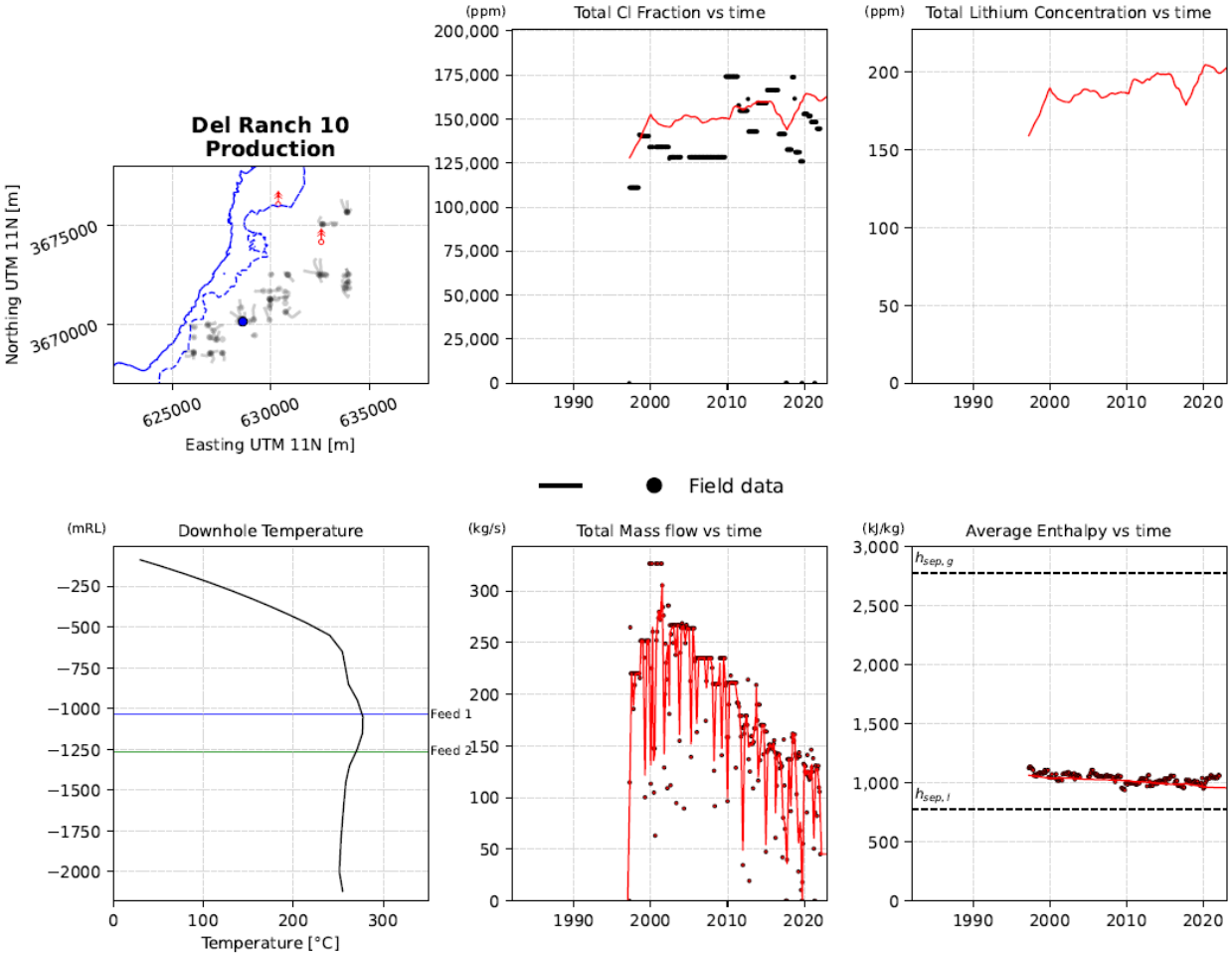

Figure 7: Production model results (solid lines) and measured data (points) for the Del Ranch 10 production well. The location of the Del Ranch 10 well is shown in blue in the map (top left) with the Salton Sea coastline (original as dashed line, current as solid line) and surface features locations indicated with red markers.

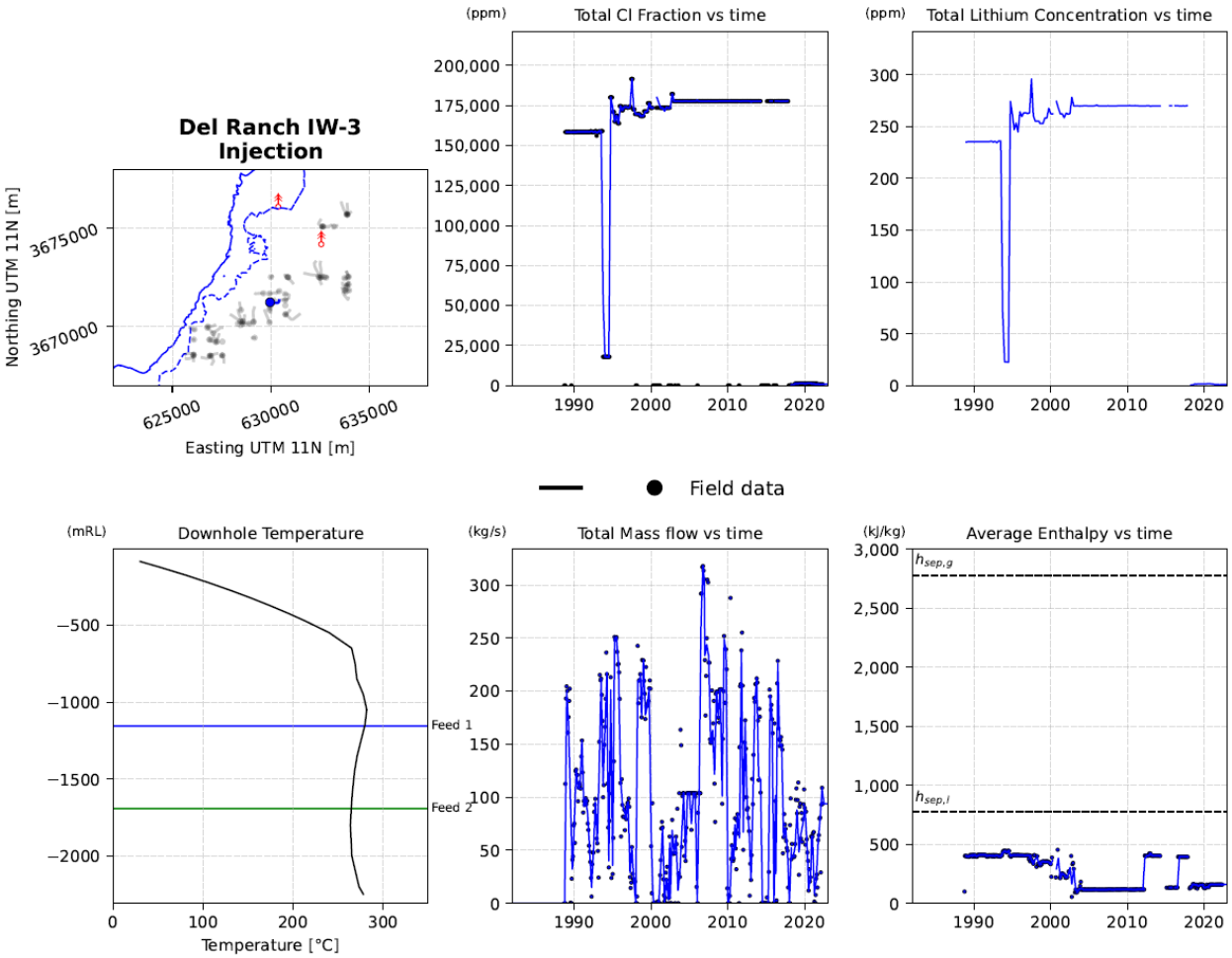

Figure 8: Production model results (solid lines) and measured data (points) for a selected reinjection well. The location of the Del Ranch IW-3 well is shown in blue in the map (top left) with the Salton Sea coastline (original as dashed line, current as solid line) and surface features locations indicated with red marker.

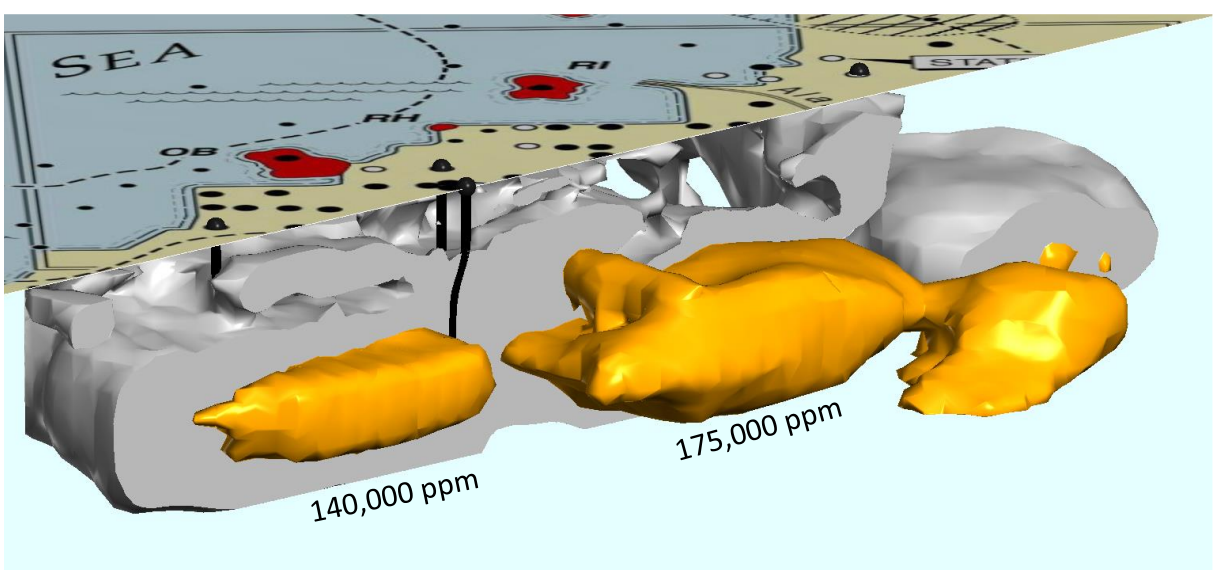

Figure 9: Chloride isosurfaces at 2023 estimated from the production model. The 140,000 ppm isosurface is cut away to reveal the 175,000 ppm isosurface.

7. FUTURE SCENARIOS

In our previous studies (Dobson et al., 2023, O'Sullivan et al., 2023a) we considered a simple future scenario to investigate the broad effect of lithium extraction on lithium production rates. The scenario assumed that all production and reinjection rates remained constant for all wells for the next 20 years. The reinjected chloride concentrations also remained constant for the full period. However, from 01/01/2024 the lithium concentration for all reinjection wells was reduced by 95%, which is representative of a future scenario where technology allows for 95% of the lithium in the brine to be extracted before reinjection. This scenario is referred to as Scenario 1.

The total amount of lithium forecast to be produced in Scenario 1 is shown in Figure . As discussed in Dobson et al. (2023) and O'Sullivan et al. (2023a) the decline in forecasted lithium production is a result of chemical breakthrough from the reinjected fluid with a low lithium concentration. Our previous studies also identified that the lithium production rates can be manipulated and optimized by planning targeted reinjection.

In this study we investigated two new scenarios with reinjection targeting the periphery of the production reservoir where high lithium concentrations have been measured. The plot in Figure shows the distribution of lithium concentrations in the production reservoir at -1250 masl at the beginning of 2023. It is interesting to note that some zones in the reservoir are predicted to have already experienced dilution of the lithium concentration. This is a result of reinjection of low lithium concentration condensate in particular wells. The new reinjection wells were planned as vertical wells with two wells per well pad, one targeting the intermediate depths of the reservoir (-1000 masl to -1400 masl) and one targeting the deep part of the reservoir (-1400 masl to -2400 masl).

For all three scenarios the existing production wells were put on to deliverability and no new production wells were added. The total amount of reinjected fluid was kept constant for all three scenarios as were the reinjection enthalpies. For Scenarios 2 and 3 a total of 36 new reinjection wells were planned, 18 targeting intermediate depths and 18 targeting the deep reservoir. In Scenario 2 the total reinjection was split evenly between the wells resulting in 360 t/h being reinjected into each well. In Scenario 3 the deep reservoir was targeted more heavily with 600 t/h reinjected into the deep wells and 120 t/h into the intermediate wells. The objective of Scenario 3 was to slow down the thermal breakthrough occurring in the more permeably intermediate layers of the production reservoir. All three scenarios were run for 20 years with the lithium extraction process beginning at the start of the second year.

The results of the scenarios are compared in Figure which shows that the amount of lithium recovered is increased significantly by moving the reinjection to the periphery of the production zone. The plot comparing total production flow rates for the three scenarios shows that the reduction in pressure support as a result of moving the reinjection is forecast to be small with total production flow rates dropping by approximately 500 t/hr. This small reduction could be alleviated by drilling additional production wells.

The results show that targeting the deep periphery of the reservoir for reinjection in Scenario 3 is forecast to slow down chemical breakthrough when compared with Scenario 2. This is achieved while maintaining very similar total production rates and enthalpies. The plots in Figure to 16 compare the forecasts of the lithium distribution in the intermediate reservoir and deep reservoir in 2030 and 2040. They clearly show the progression of the dilute lithium reinjected fluid over time in each case and highlight the effectiveness of reinjecting on the periphery of the production zone. Plots b) and c) in Figure and 15 also highlight how reducing reinjection rates into the high permeability intermediate production reservoir slows the chemical breakthrough in Scenario 3 compared with Scenario 2.

Similarly, plots b) and c) in Figure and 16 show that in spite of the increased deep reinjection rate in Scenario 3, the chemical breakthrough in the deep reservoir is still not severe by 2040.

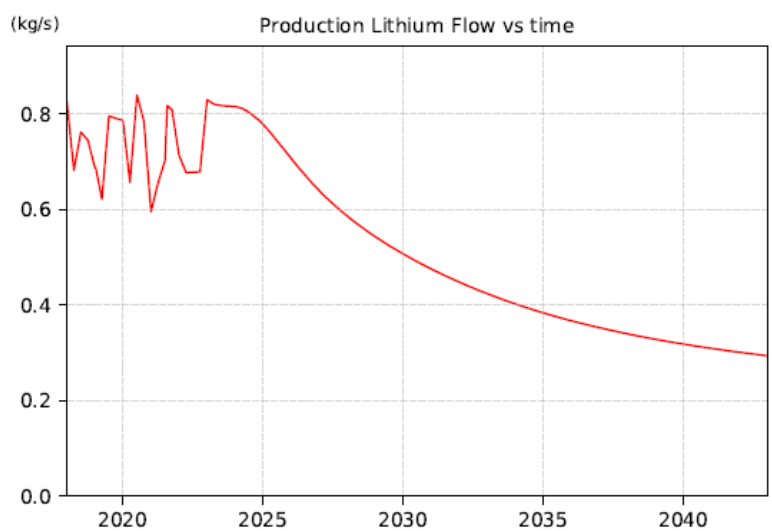

Figure 10: Forecast total lithium production rate for Scenario 1.

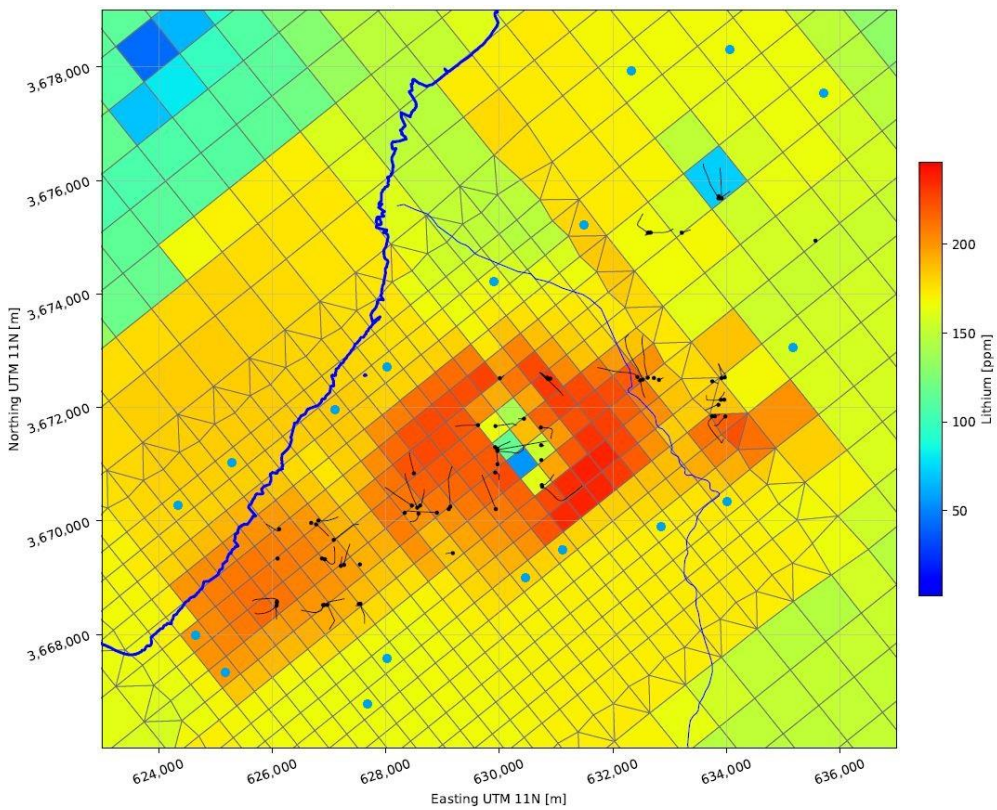

Figure 1: Forecast lithium concentration at -1250 masl at the beginning of 2023. The existing wells are shown in black, the current edge of the Salton Sea and the Alamo River in dark blue and the proposed new reinjection wells in light blue.

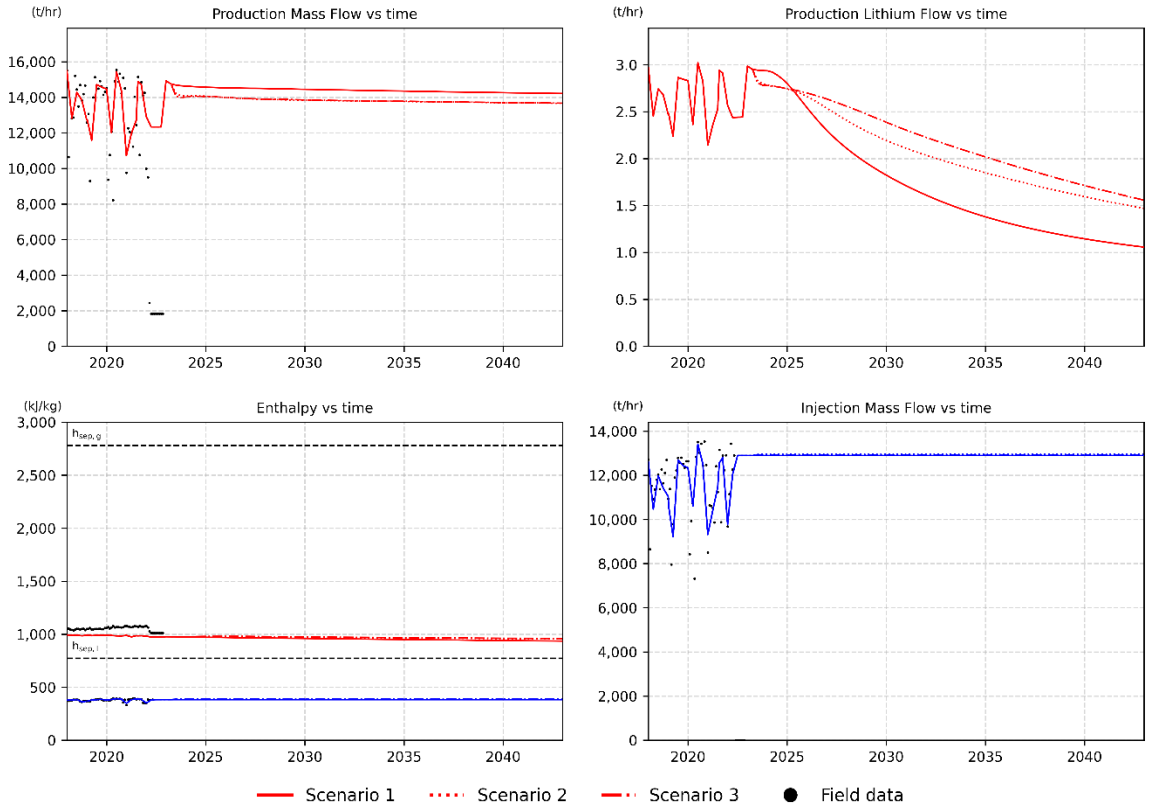

Figure 2: Comparison of forecast total flow rates for the three scenarios.

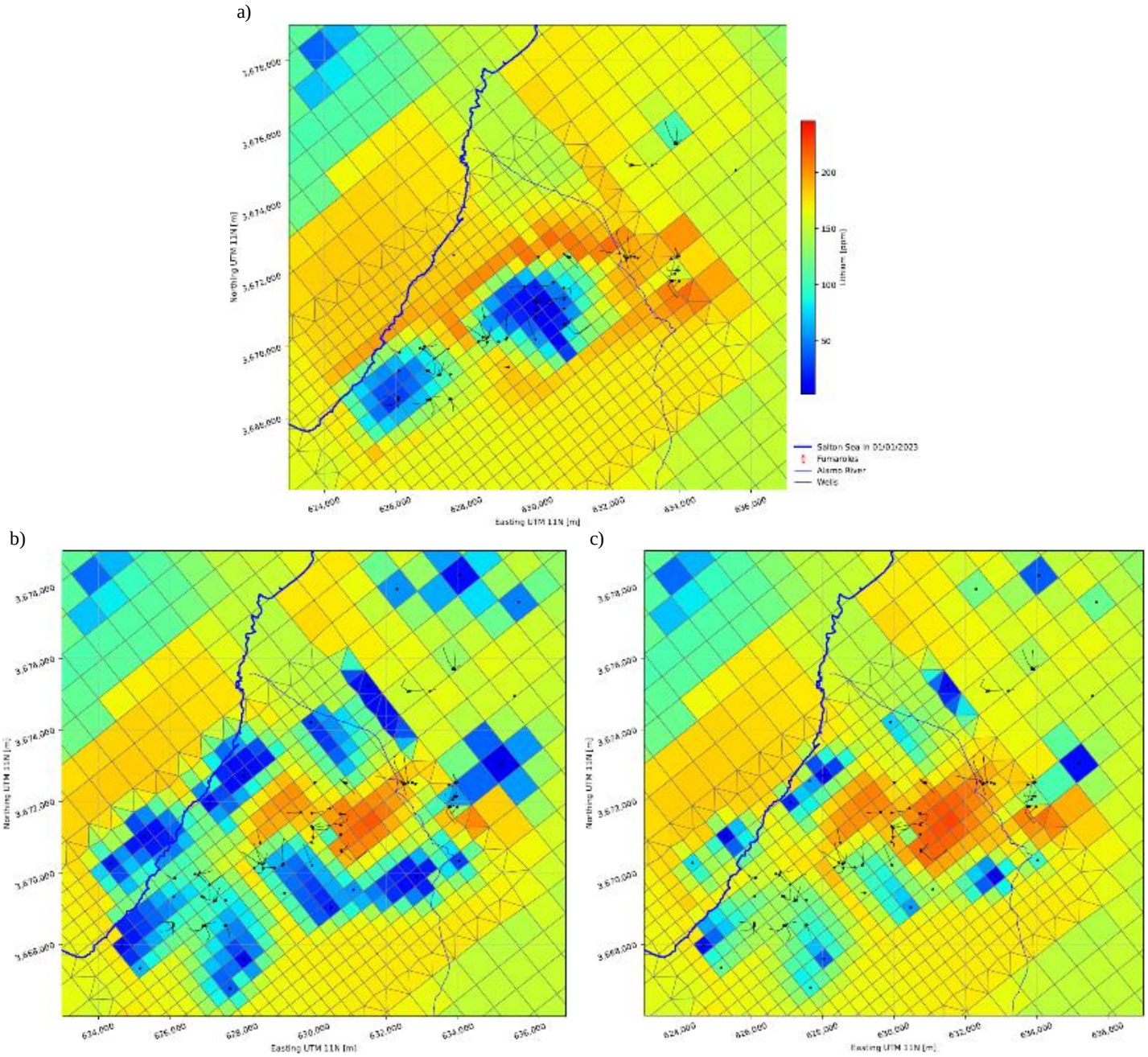

Figure 3: Comparison of forecast lithium distribution in the intermediate reservoir at -1250 masl in 2030 for a) Scenario 1, b) Scenario 2 and c) Scenario 3.

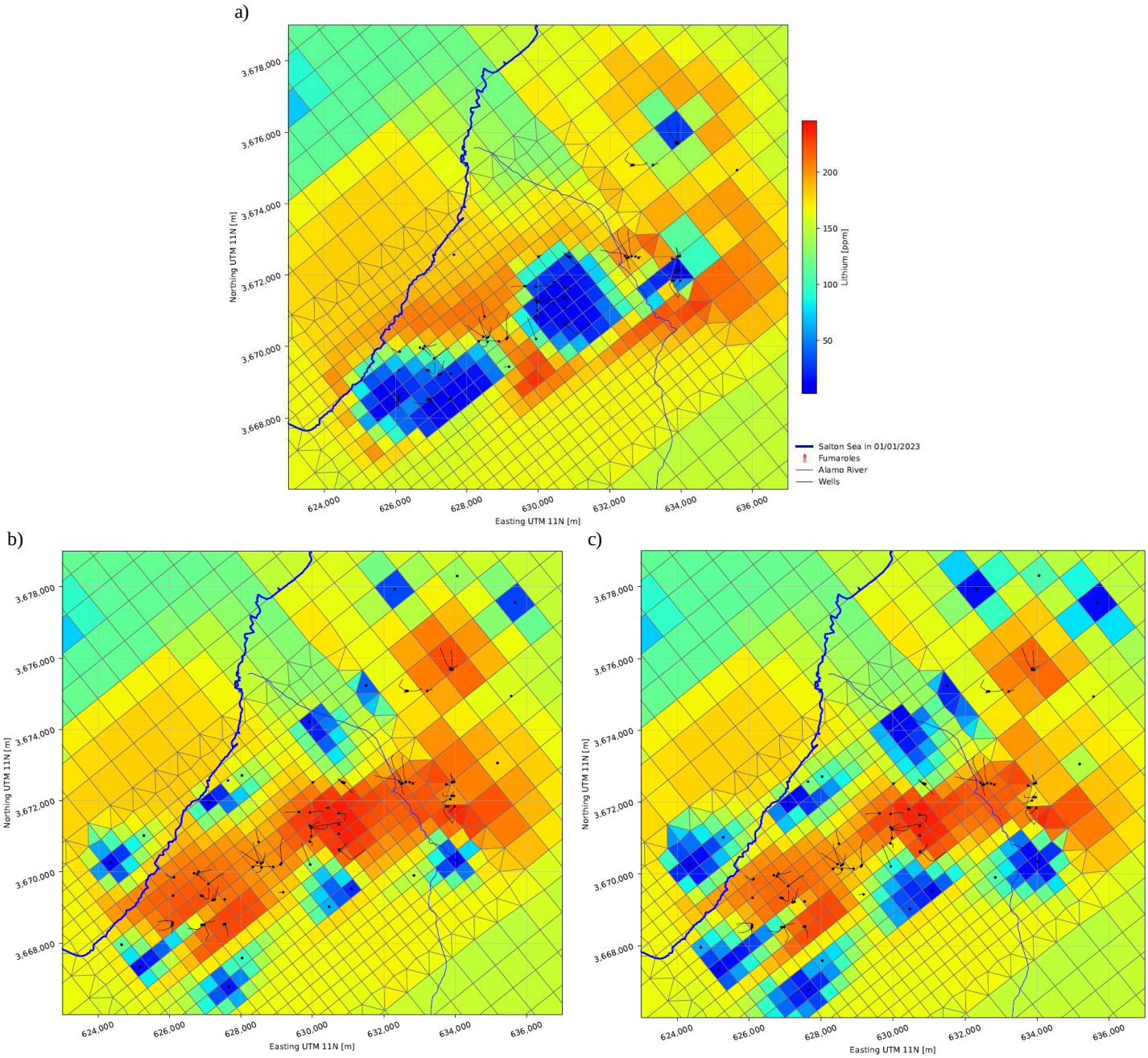

Figure 4: Comparison of forecast lithium distribution in the deep reservoir at -2000 masl in 2030 for a) Scenario 1, b) Scenario 2 and c) Scenario 3.

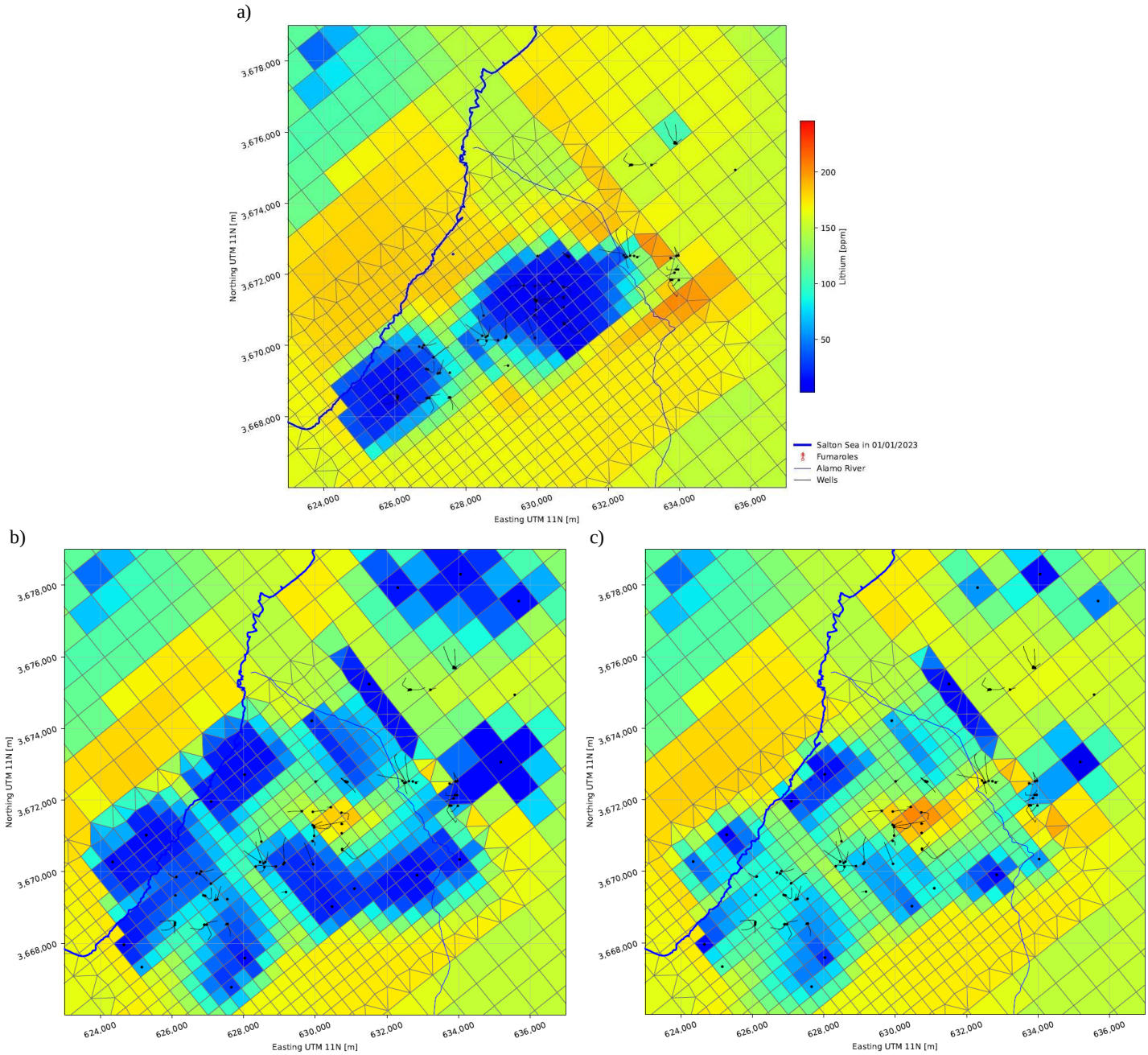

Figure 5: Comparison of forecast lithium distribution in the intermediate reservoir at -1250 masl in 2040 for a) Scenario 1, b) Scenario 2 and c) Scenario 3.

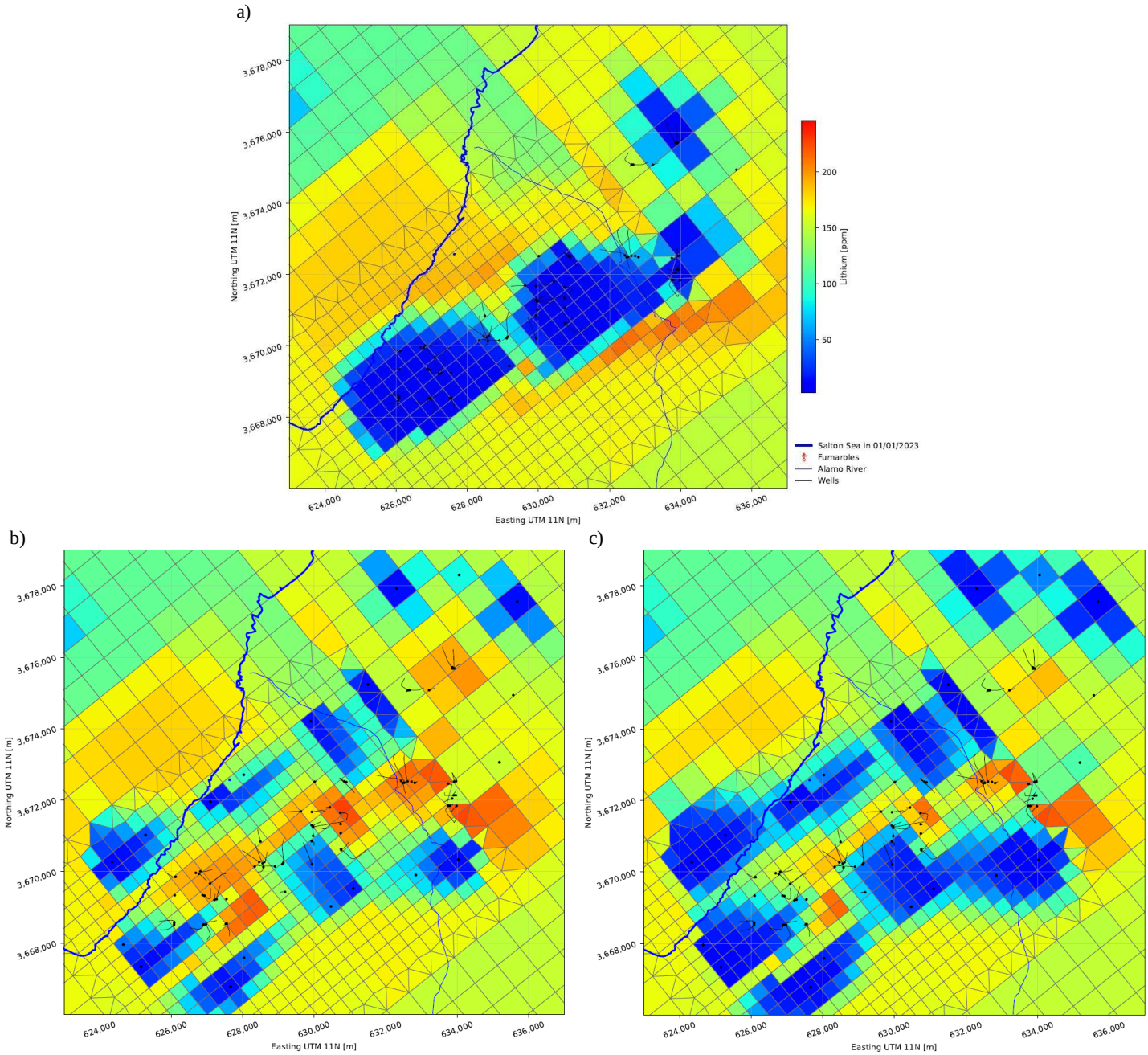

Figure 6: Comparison of forecast lithium distribution in the deep reservoir at -2000 masl in 2040 for a) Scenario 1, b) Scenario 2 and c) Scenario 3.

The objective of these scenarios was to demonstrate the ability to manipulate the rates of lithium production without adversely affecting energy production by optimizing reinjection targets. The total amounts of lithium extracted over the 19 years of production are given in Table 2 for all three scenarios. It shows that Scenario 3 is forecast to provide nearly 30% more lithium compared with Scenario 1 by optimizing the reinjection targets.

Table 2: Total forecast lithium extracted for each scenario over 19 years of production.

Scenario	Forecast Lithium Extracted (kg)
1	278,000,000
2	338,000,000
3	360,000,000

As discussed above, none of the scenarios considered additional production wells. Optimising both production and reinjection targets will certainly enable higher production rates of both lithium and energy to be achieved. However, this was outside the scope of this project and will be considered following model refinement and recalibration which is currently underway.

8. CONCLUSIONS

This modelling study investigated the use of targeted reinjection strategies to extract lithium efficiently from the SSGF. The results show that the production rates of lithium can be increased by nearly 30% by moving reinjection to the periphery of the production zone and preferentially targeting deep reinjection. Improved lithium extraction rates were achieved without sever impacts on energy production rates.

The study did not consider the economic viability of moving reinjection on a large scale at the SSGF and this issue must be addressed as part of further investigations. Similarly, this study did not consider changes or increases in production rates which also will affect the rates of lithium production and the overall economics of the project.

More detailed extraction scenarios will be investigated and optimized following refinement and recalibration of our current model. Uncertainty quantification will also be carried out to provide more robust forecasts and support decision-making in the future.

ACKNOWLEDGEMENTS

The authors would like to thank the Lawrence Berkeley National Laboratory and the Department of Energy's Geothermal Technologies Office for supporting this project. The authors would also like to thank Seequent for their ongoing collaboration and support.

REFERENCES

Araya, N. and O'Sullivan, J. "A 3D Conceptual and Natural-State Model of the Salton Sea Geothermal Field." GRC Transactions, 46, (2022). 2123-2155.

CalGEM. "GeoSteam: Geothermal Well Records, Production and Injection Data [Data Files]." (2022). https://geosteam.conservation.ca.gov/

California Department of Conservation. "Geological Map of California [Data File]." (2015). https://maps.conservation.ca.gov/cgs/#datalist

California Department of Conservation. "Geothermal Production and Injection Data [Salton Sea]." (2022). https://www.conservation.ca.gov/calgem/geothermal/manual

Croucher, A., O'Sullivan, M., O'Sullivan, J., Yeh, A., and Burnell, J. "Waiwera: A parallel open-source geothermal flow simulator." Computers and Geosciences, 141, (2020).

de Beer, A., Gravatt, M., Renaud, T., Nicholson, R., Maclaren, O. J., Dekkers, K., O'Sullivan, M., O'Sullivan, J., "Geologically Consistent Prior Parameter Distributions for Uncertainty Quantification of Geothermal Reservoirs." 48th Stanford Workshop on Geothermal Reservoir Engineering, California, (2023).

Dekkers, K., Gravatt, M., Maclaren, O. J., Nicholson, R., Nugraha, R., O'Sullivan, M., O'Sullivan, J., "Resource Assessment: Estimating the Potential of a Geothermal Reservoir." 47th Stanford Workshop on Geothermal Reservoir Engineering, California, (2022).

Dobson, P., Araya, N., Brounce, M., Busse, M., Camarillo, M. K., English, L., ... & White, M. (2023). Characterizing the Geothermal Lithium Resource at the Salton Sea. Lawrence Berkeley National Laboratory (LBNL), Berkeley, USA.

Dorsey, R. "Stratigraphy, Tectonics, and Basin Evolution in the Anza-Borrego Desert Region." In G. T. Jefferson and L. Lindsay, Fossil Treasures of the Anza-Borrego Desert, Sunbelt Publication, (2006) 89-104.

Han, L., Hole, J.A., Stock, J.M., Fuis, G.S., Kell, A., Driscoll, N.W., Kent, G.M., Harding, A.J., Rymer, M.J., González-Fernández, A., and Lázaro-Mancilla, O. "Continental rupture and the creation of new crust in the Salton Trough rift, Southern California and northern Mexico: Results from the Salton Seismic Imaging Project." Journal of Geophysical Research: Solid Earth, 121, (2016), 7469-7489.

Hulen, J., Kaspereit, D., Norton, D.L., Osborn, W., Pulka, F.S. "Refined Conceptual Modeling and a New Resource Estimate for the Salton Sea Geothermal Field, Imperial Valley, California." Geothermal Resources Council Transactions, 26, (2002), 29-36.

Hulen, J., Norton, D., Kaspereit, D., Murray, L., Van de Putte, T., and Wright, M. "Geology and a Working Conceptual Model of the Obsidian Butte (Unit 6) Sector of the Salton Sea Geothermal Field, California." GRC Transactions, 27, (2003), 227-240.

Kaspereit, D., Mann, M., Sanyal S., Rickard, B., Osborn, W., and Hulen, J. "Updated Conceptual Model and Reserve Estimate for the Salton Sea Geothermal Field, Imperial Valley, California." GRC Transactions, 40, (2016), 57-66.

Kirby, S.M., Janecke, S.U., Dorsey, R.J., Housen, B.A, Langenheim, V.E., McDougall, K.A., and Steely, A.N. "Pleistocene Brawley and Ocotillo Formations: Evidence for Initial Strike-Slip Deformation Along the San Felipe and San Jacinto Fault Zones, Southern California." Journal of Geology, 115, (2007).

Lachenbruch, A.H., Sass, J.H., and Galanis, S.P. Jr. "Heat flow in southernmost California and the origin of the Salton Trough." Journal of Geophysical Research, 90 (B8), (1985), 6709-6736.

Lynch, D.K., and Hudnut, K.W. "The Wister Mud Pot Lineament: Southeastward Extension or Abandoned Strand of the San Andreas Fault?" Bulletin of Seismological Society of America, 98, (2008), 1720-1729.

Marshall, S., Plesch, A., Shaw, J., and Nicholson, C. "SCEC Community Fault Model v. 5.3.2." (2022). https://www.scec.org/research/cfm-viewer/

Mazzini, A., Svensen, H., Etiope, G., Onderrdonk, N., and Banks, D. "Fluid origin, gas fluxes and plumbing system in the sediment-hosted Salton Sea geothermal system (California, USA)." Journal of Volcanology and Geothermal Research, 205, (2011), 67-83.

Meidav, T., West, R., Katzenstein, A., and Rostein, Y. "An Electrical Resistivity Survey of the Salton Sea Geothermal Field, Imperial Valley California." Lawrence Livermore Laboratory, UCRL-13690, (1976).

McKibben, M.A., Elders W.A., and Raju A.S.K. "Crisis at the Salton Sea: Lithium and Otherm Geothermal Mineral and Energy Resources Beneath the Salton Sea." Crisis at the Salton Sea: The Vital Role of Science, University of California Riverside Salton Sea Task Force, (2021), 74-85.

McKibben, M. A., and Hardie, L. A. "Ore-forming brines in active continental rifts." Geochemistry of Hydrothermal Ore Deposits, 3rd Edition, (1997), 875–933.

McKibben, M.A., Williams, A.E., Elders, W.A., and Eldridge, C.S. "Saline brines and Metallogenesis in a Modern Sediment-filled Rift: the Salton Sea Geothermal system, California, U.S.A." Applied Geochemistry, 2, (1987), 563-578.

McGuire, J.J., Lohman, R.B., Catchings, R.D., Rymer, M.J., and Goldman, M.R. "Relationships Among Seismic Velocity, Metamorphism, and Seismic and Aseismic Fault Slip in the Salton Sea Geothermal Field region." Journal of Geophysical Research, 120, (2015), 2600-2615.

Nichols, E. "Geothermal Exploration Under the Salton Sea Using Marine Magnetotellurics." California Energy Commission, PIER Renewable Energy Technologies Program, CEC-500-2009-005, (2009).

Norton and Hulen. "Magma-Hydrothermal Activity in the Salton Sea Geothermal Field Imperial County, California." GRC Transactions, 30, (2006). 991-998.

Omagbon, J., Doherty, J., Yeh, A., Colina, R., O'Sullivan, J., McDowell, J., . . . O'Sullivan, M. "Case studies of predictive uncertainty quantification for geothermal models." Geothermics. 97, (2021), 102263.

Rao, A.P. "The hydraulic connectivity, perennial warming and relationship to seismicity of the Davis-Schrimpf seep field, Salton Trough, California from new and recent temperature time-series." M.S. thesis, California State University, Long Beach, (2016), 107 p.

Svensen, H., Karlsen, D.A., Sturz, A., Backer-Owe, K., Banks, D.A., and Planke, S. "Processes Controlling Water and Hydrocarbon Composition in Seeps from the Salton Sea Geothermal System, California, USA." Geology, 35, (2007), 85-88.

O'Sullivan, J., Araya, N., Popineau, J., Renaud, T., and Riffault, J. "An EWASG Natural State and Production Forecast Model of the Salton Sea Geothermal Field." GRC Transactions, 47, (2023).

O'Sullivan, M., Pruess, K., and Lippmann, M. "Geothermal Reservoir Simulation: The state-of Practice and Emerging trends." Proceedings World Geothermal Congress, (2000).

O'Sullivan, M., & O'Sullivan, J. "Reservoir Modeling and Simulation for Geothermal Resource Characterization and Evaluation." Geothermal Power Generation, (2016), 165-199.

O'Sullivan, J.P., Araya, N., Popineau, J., Renaud, T., & Jeremy Riffault, J. "An EWASG Natural State and Production Forecast Model of the Salton Sea Geothermal Field", Transactions GRC, 47 (2023a).

O'Sullivan, J., Popineau, J., Gravatt, M., Renaud, T., Riffault, J., Croucher, A., Yeh, A. & O'Sullivan M. "An integrated, mesh-independent geothermal modeling framework." Environmental Modeling and Software, 163, (2023b), 105666.

Palmer, T.D. "Characteristics of Geothermal Wells Located in the Salton Sea Geothermal Field, Imperial County, California." Lawrence Livermore Laboratory, UCRL-51976, (1975).

Popineau, J., O'Sullivan, J., O'Sullivan, M., Archer, R., and Williams, B. "An integrated Leapfrog/TOUGH2 Workflow for a Geothermal Production Modeling." 7th African Rift Geothermal Conference, (2018).

Sass, J.H., Galanis, S.P., Jr., Lachenbruch, A.H., Marshall, B.V., and Munroe, R.J. "Temperature, Thermal Conductivity, Heat Flow, and Radiogenic Heat Production from Unconsolidated Sediments of the Imperial Valley, California." USGS Open File Report, 84-490, (1984).

Sass, J.H., Priest, S.S., Duda, L.E., Carson, C.C., Hendricks, J.D., and Robison, L.C. "Thermal Regime of the State 2-14 well, Salton Sea Scientific Drilling Project." Journal of Geophysical Research, 93 (B11), (1988), 12,995-13,004.

Williams, A.E., and McKibben, M.A. "A Brine Interface in the Salton Sea Geothermal System California: Fluid Geochemical and Isotopic Characteristics." Geochimica et Cosochimica Acta, 53, (1989), 1905-1920.

Younker, L.W., Kasameyer, P.W., and Tewhey, J.D. "Geological, Geophysical, and Thermal Characteristics of the Salton Sea Geothermal Field, California." Journal of Volcanology and Geothermal Research, 12, (1981), 221-258.